Supplemental Material

Equation of State and Thermometry of the 2D SU(N) Fermi-Hubbard Model

G. Pasqualetti,[1,2,3,*] O. Bettermann,[1,2,3] N. Darkwah Oppong,[1,2,3] E. Ibarra-García-Padilla,[4,5,6,7] S. Dasgupta,[4,5] R. T. Scalettar,[6] K. R. A. Hazzard,[4,5,6] I. Bloch,[1,2,3] and S. Fölling[1,2,3]

[1] *Ludwig-Maximilians-Universität, Schellingstraße 4, 80799 München, Germany*
[2] *Max-Planck-Institut für Quantenoptik, Hans-Kopfermann-Straße 1, 85748 Garching, Germany*
[3] *Munich Center for Quantum Science and Technology (MCQST), Schellingstraße 4, 80799 München, Germany*
[4] *Department of Physics and Astronomy, Rice University, Houston, Texas 77005-1892, USA*
[5] *Rice Center for Quantum Materials, Rice University, Houston, Texas 77005-1892, USA*
[6] *Department of Physics, University of California, Davis, California 95616, USA*
[7] *Department of Physics and Astronomy, San José State University, San José, California 95192, USA*

(Dated: December 2, 2023)

CONTENTS

S.I. EXPERIMENTAL TECHNIQUES

A. State preparation

Our experiment starts by loading a spin-balanced unpolarized mixture ($N = 6$) of approximately 1.6×10^6 ^{173}Yb atoms from a magneto-optical trap into a crossed optical dipole trap (XODT), where we perform forced evaporation to $T/T_F^{3D} < 0.2$. We then perform a second stage of evaporation with an optical gradient, leading to an ensemble of $N_p \approx 2 \times 10^3$ atoms in the central plane of a vertical lattice with wavelength $\lambda = 759.3\,\mathrm{nm}$ and lattice spacing $d_{\mathrm{vert}} = 3.9(3)\,\mu\mathrm{m}$. The vertical band gap is $3.95(1)\,\mathrm{kHz}$, determined from a measurement of the $0 \to 2$ band resonance with parametric modulation. In this configuration, the coefficients of the harmonic confinement are $(\kappa_x, \kappa_y)d^2 = [1.35(3), 2.23(6)] \times h$. Numerical simulations [1] predict that for $N_p \lesssim 5 \times 10^3$, nearly all the atoms should be loaded in the single central plane of the lattice. We verify this assumption with a momentum refocussing technique similar to the one described in Ref. [2].

Mixtures with $N = 4$ are prepared in the XODT before the evaporation by optically pumping the population of the two nuclear spin states $m_F \in \{\pm 1/2\}$ to the other spin states with four circularly-polarized pulses on the $^1\mathrm{S}_0 \to {}^3\mathrm{P}_1$ intercombination line at 50 G. Mixtures with $N = 3$ are prepared in a similar fashion by pumping the spin components $m_F \in \{\pm 1/2, -3/2\}$ to the other states with five pulses. In both cases, we check the balancing of the spin components with an Optical Stern-Gerlach (OSG) technique in time of flight [3]. The standard deviation of the population of the selected spin components is below 5 % per component for SU(6) and SU(3) and below 8 % for SU(4). The residual fraction of unwanted spin components is below 5 % per component.

B. Lattice loading and Hubbard parameters

The two orthogonal in-plane lattices have the same depth and they are tuned to the desired value following the ramp profile shown in Fig. S1. The ramp speed has been chosen to minimize the entropy in the round-trip experiment. After reaching the desired lattice depth, we quickly switch off the vertical lattice to avoid light-assisted collisions and to perform in situ imaging.

We calibrate the lattice depths along the two directions by measuring the band gap between the lowest and the second excited band with parametric modulation. U and t are obtained by numerically solving the band structure for the measured band gap and U is calculated as the Wannier overlap in the lowest band [4]. The values of the relevant Hubbard parameters for this work are re-

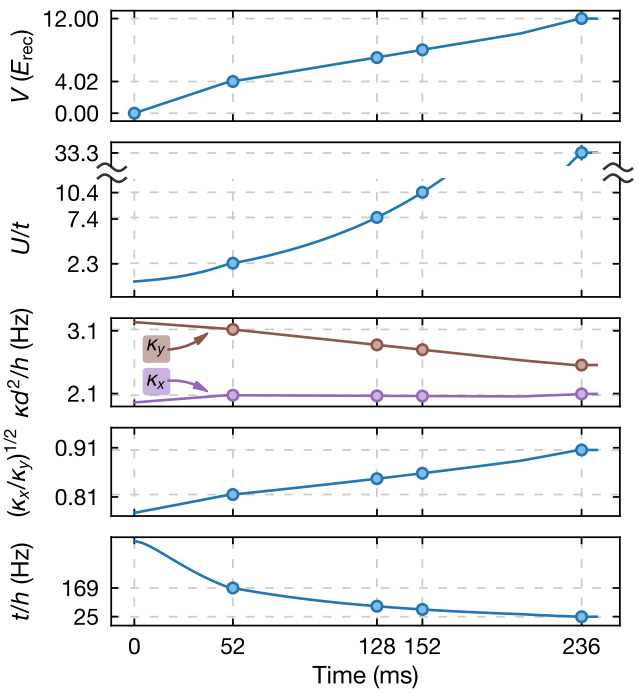

FIG. S1. Time dependence of the lattice depth V and the Hubbard parameters U, κ_x, κ_y and t during the lattice ramps. The lattice depth and the hopping along the spatial x and y directions are the same.

ported in Tab. S1. We cross-check the calculation by directly measuring U with modulation spectroscopy for $V = 13\,E_{\rm rec}$ ($U/t \approx 43$) and $19\,E_{\rm rec}$ ($U/t \approx 178$). For this measurement, we first tune the lattice depth to the desired value. We then modulate the depth of both lattices with an amplitude of 2 % to 6 % and at the same time apply the pair removal pulse. For modulation frequencies resonant with U, atom losses are enhanced. For $13\,E_{\rm rec}$, we measure $U = h \cdot 886(8)$ Hz for an expected value of $h \cdot 856(8)$ Hz. For $19\,E_{\rm rec}$, we measure $U = h \cdot 1065(8)$ Hz for an expected value of $h \cdot 1069(9)$ Hz (Fig. S2).

C. Pair removal

The pair-removal operation is performed with a photoassociation beam working on the $^1S_0 \rightarrow {}^3P_1$ intercombination line, resonant with a molecular transition detuned by $-599.28(8)$ MHz with respect to the single-particle transition with a bias magnetic field of 1 G. The beam is coplanar with the lattices and has a power of 30 mW. For pair removal, we first ramp the lattice to the desired U/t value according to the ramps described in Sec. S.I B, quench the depth to $30\,E_{\rm rec}$ in 0.5 ms and then apply the photoassociation pulse for 10 ms.

U/t	V ($E_{\rm rec}$)	U/h (Hz)	t/h (Hz)	$\kappa_x d^2/t\,(10^{-3})$	$\kappa_y d^2/t\,(10^{-3})$
2.3(1)	4.0(1)	398(6)	170(4)	10(1)	13(1)
7.5(4)	7.1(1)	582(9)	78(3)	26(1)	35(1)
10.4(6)	8.0(2)	634(9)	61(2)	38(1)	50(1)
33(2)	12.0(2)	816(11)	25(1)	135(1)	174(1)

TABLE S1. Hubbard parameters for our system. V is the lattice depth along one direction (both lattices have the same depth). For $U/t = 2.3(1)$, the next-nearest-neighbor hopping is $h \cdot 12$ Hz.

The on-site atom number after pair removal is:

$$n_{\rm PR} = \sum_{\alpha=1}^{N} (\alpha \bmod 2)\, p_\alpha, \tag{S.1}$$

where p_α is the probability of having α particles on a given site (αp_α is the average number of particles on a site with occupation α and $n = \sum_{\alpha=0}^{N} \alpha p_\alpha$) and we neglect the tunneling during the quench. We correct Eq. S.1 to take into account the experimental imperfections of the photoassociation beam:

$$\tilde{n}_{\rm PR} \simeq e^{-\gamma_s t}\left[\sum_\alpha (\alpha \bmod 2)\, p_\alpha + e^{-\gamma_d t}\left(\sum_\alpha 2\,\lfloor \alpha/2 \rfloor p_\alpha\right)\right], \tag{S.2}$$

where $\lfloor\cdot\rfloor$ represents the floor function, γ_s and $\gamma_s + \gamma_d$ represent the decay rate of the singlons and the doublons and we neglect the fast decay of the states with more than two particles per site [5]. For $\gamma_s, \gamma_d \rightarrow 0$ we recover $\tilde{n}_{\rm PR} \rightarrow n_{\rm PR}$.

Efficiency calibration

We calibrate the efficiency of the pair removal by looking at the atom losses as a function of the pulse duration in the deep Mott insulating regime [$U/t = 33(2)$]. Neglecting the sites occupied by more than two particles, we fit a double-exponential model:

$$N_p = e^{-\gamma_s t}\left(N_s + N_d e^{-\gamma_d t}\right), \tag{S.3}$$

where $N_p = N_s + N_d$ is the total atom number, N_s the number of singlons, N_d the number of doublons. We obtain $1/\gamma_d = 1.2(2)$ ms and $1/\gamma_s = 200(11)$ ms, which we find to be independent of N inside the uncertainties (see Fig. S3). We cross-checked the value of γ_s by repeating the same experiment in a small Mott insulator with $\approx 1 \times 10^3$ atoms and no doublons (inset of Fig. S3). For a pulse duration of 10 ms, we remove all the doublons within our detection sensitivity and about 5 % of the singlons. We take this into account when calculating the theory curves in Fig. 2.

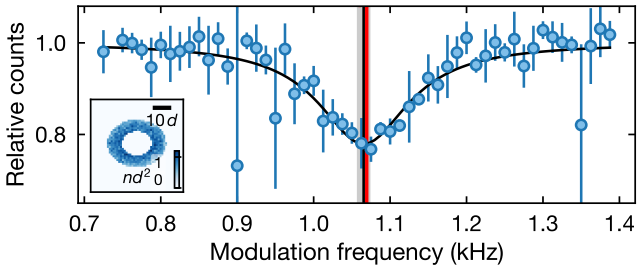

FIG. S2. Direct measurement of U with modulation spectroscopy for $U/t \approx 178$. Red line: expected value of U according to the Wannier overlap. Black line: fit of a Lorentzian function. To enhance the signal-to-noise ratio, data have been evaluated in an elliptical shell where the cloud is mainly in the insulating phase (inset).

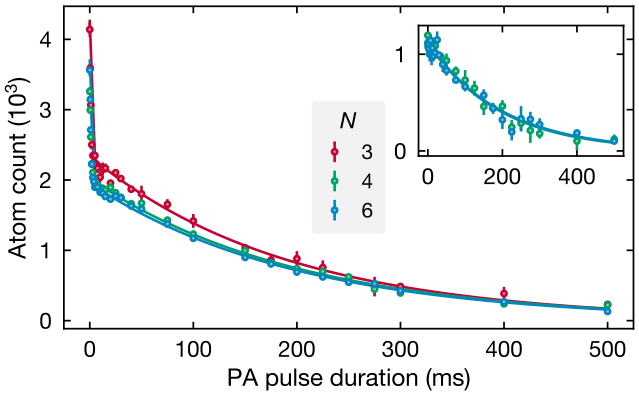

FIG. S3. Calibration of the photoassociation beam. Atom number as a function of the pulse duration for $N = 3$ (red), $N = 4$ (green) and $N = 6$ (blue). We first tune the lattice depth to $12\,E_{\rm rec}$ [$U/t = 33(2)$] and then quench it to $30\,E_{\rm rec}$ before applying the photoassociation pulse. Inset: Same experiment repeated for a smaller atom number, such that $nd^2 \simeq 1$ in the center.

D. Characterization of the potential

1. *Trap frequencies*

Across the region sampled by the atomic cloud, the confinement due to the Gaussian lattice beams is approximately harmonic, such that $\mu(x,y) = \mu_0 - \frac{1}{2}\left(\kappa_x x^2 + \kappa_y y^2\right)$. The two coefficients are determined by a fit of the EoS for each lattice depth with free parameters $T/t, \mu_0/t, \kappa_x d^2/t, \kappa_y d^2/t$. We verify that the fourth order anharmonic correction coming from the Gaussian profile, calculated for the measured beam waist and power of the beams, is negligible for the size of the cloud. However, the values obtained for κ_x and κ_y do not fully agree with the independent measurement of the frequency of the oscillatory motion of the atoms in the combined potential. More specifically, we load a spin-polarized cloud in the combined potential of the vertical lattice and one in-plane lattice at a time. We measure the center of mass (COM) oscillation after an initial displacement of about $5\,d$ along the lattice direction and we verify that the Rayleigh range contribution to the combined potential is negligible. A comparison between the two sets of values can be found in Fig. S4.

2. *Fit comparisons*

A possible explanation for the discrepancy in the shape of the inferred potential described in Sec. S.I D 1 might be a lack of adiabaticity and equilibration during the tuning of U/t. However, the temperature measured with the fluctuation-dissipation theorem matches the one obtained from the fit of the EoS. This is not the case if we use the chemical potential coming from the oscillatory-motion calibration. In particular, we verify that for this potential, $N = 6$ and $U/t = 33(2)$ we obtain a temperature inside the regime of convergence of our theory models when we use the FDT, but which does not quantitatively match the temperature returned by the fit of the EoS with the same potential.

Moreover, we verify that the values of κ_x and κ_y determined by the EoS fit are robust against atom number variation (see Fig. S5).

Finally, we observe that κ_x and κ_y are also insensitive to the lattice ramp time duration. In Fig. S6 we show a test which consists of tuning the lattice depth of an SU(6) sample from zero to $13\,E_{\rm rec}$ ($U/t \approx 44$) with a linear ramp of different durations Δt between 300 ms and 1 s. For each Δt, we fit the EoS with second-order high-temperature series expansion (HTSE-2) and leave (T/t, $\kappa_x d^2/t$, $\kappa_y d^2/t$, μ_0/t) as free fit parameters. We observe that the values of κ_x and κ_y returned by the fit for different Δt are compatible among each other [$\kappa_x d^2/t = 0.151(2)$, $\kappa_y d^2/t = 0.204(3)$]. However, they are incompatible with the ones predicted by the independent "oscillatory-motion" calibration described in Sec. S.I D 1 ($\kappa_x^{\rm osc} d^2/t \simeq 0.109$, $\kappa_y^{\rm osc} d^2/t \simeq 0.131$). If we use these values for the fit, it fails for $\Delta t = 0.3$ s and 0.5 s and it returns high residuals for $\Delta t = 1$ s, failing to reproduce the cloud shape especially in the center [Fig. S6(c)]. We conclude that if the mismatch between the two different harmonic potential parameters comes from a lack of equilibration during the tuning of the lattice depth, the time scale to achieve this equilibration significantly exceeds the experimentally accessible timescales.

3. *Anharmonicities*

We characterize the anharmonic corrections of the potential by an ensemble with a high temperature $T \gg t$ into the lattice and applying the atomic limit model with

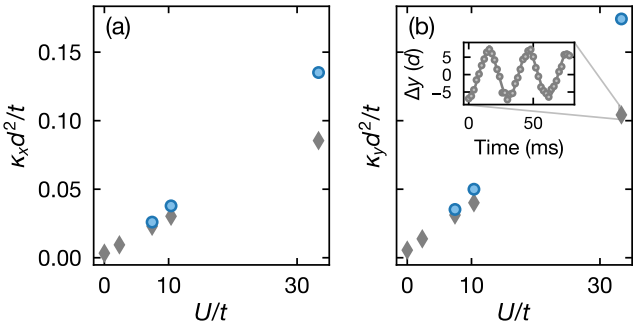

FIG. S4. Coefficients of the harmonic confinement along the lattice axes (x, y). Circles correspond to the harmonic confinement according to the EoS fit described in the text. Diamonds correspond to an independent calibration measuring the frequencies of the COM oscillations around the center of the trap. Inset: example of COM oscillations for $U/t = 33(2)$.

$t = 0$. In this way, we can generate a spatial map of the chemical potential and observe that the functional modeling as a harmonic trap is a good approximation. In particular, we estimate the anharmonic corrections being less than $0.03\,\mu_0$ over the whole region of interest in the deep Mott insulating regime.

E. Imaging techniques

We use saturated in situ absorption imaging on the stretched $^1S_0 \rightarrow {}^1P_1$ transition with circularly polarized light in the presence of a small magnetic field offset $\simeq 1$ G and a pulse duration of 5 µs. We determine the density with the modified Lambert-Beer law [6], which accounts for the high-intensity effects:

$$n(x,y) = \frac{1}{\sigma}\left[\log\left(\frac{I_{\rm in}}{I_{\rm out}}\right) + \frac{I_{\rm in} - I_{\rm out}}{I_{\rm sat}^{\rm eff}}\right], \qquad \text{(S.4)}$$

where $n(x, y)$ is the density at pixel position (x, y) and $I_{\rm in} = I_{\rm in}(x, y)$ and $I_{\rm out} = I_{\rm out}(x, y)$ are respectively the incident light and the light after absorption. We calibrate the effective saturation intensity $I_{\rm sat}^{\rm eff}$ by varying $I_{\rm in}/I_{\rm sat}$ between 2 and 8 (where $I_{\rm sat} = \pi hc\Gamma/(3\lambda^3) \simeq 60\,{\rm mW/cm^2}$ is the saturation intensity of the transition with wavelength λ and linewidth Γ) and minimizing the variation of the density profile as described in Ref. [6]. We find $I_{\rm sat}^{\rm eff}/I_{\rm sat} = 3.0(2)$ with variations of less than 5% between spin mixtures. We obtain compatible values in the 3D dipole trap, in the 2D bulk and in the deep Mott insulating regime with variations smaller than 5%. The effective cross section σ is calibrated for each spin mixture by determining the minimum of the compressibility $\kappa = \partial n/\partial\mu$ near the insulating regime at $nd^2 \simeq 1$ (see also Fig. S10). We obtain $\sigma/\sigma_0 = [0.310(3), 0.320(3), 0.321(3)]$ respectively for $N = [3, 4, 6]$, where $\sigma_0 = 3\lambda^2/(2\pi)$ is the photon resonant cross section. As an independent measurement, we extract the effective cross section from the density shot noise of a thermal sample in the 2D bulk according to the method described in Ref. [7]. In particular we make use of the fact that $\langle|\delta n_0(\mathbf{k})|^2\rangle$ is proportional to $\sigma N_p \mathcal{M}^2(\mathbf{k})$, where δn_0 are the measured local density fluctuations per pixel, $\mathbf{k}$ is a vector in Fourier space, N_p is the total atom number and $\mathcal{M}(\mathbf{k})$ is the modulation transfer function of the imaging system. By modeling $\mathcal{M}$ with aperture, intensity attenuation and aberrations as free fit parameters, we determine both σ and $\mathcal{M}$ [7]. We obtain $\sigma/\sigma_0 = [0.35(1), 0.38(1), 0.384(7)]$ respectively for $N = [3, 4, 6]$. We attribute the differences between the values to cooperative optical response effects at high densities [8, 9].

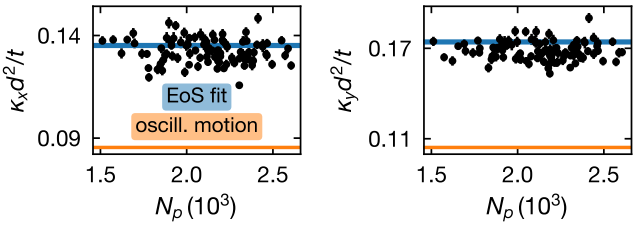

FIG. S5. Dependency of κ_x and κ_y with the atom number N_p. Each point corresponds to a single realization with $N = 6$ and $U/t = 33(2)$. For each realization we fit $(T/t,\ \kappa_x d^2/t,\ \kappa_y d^2/t,\ \mu_0/t)$ with NLCE. Blue lines: values used in the main text for this U/t ratio. Orange lines: values determined with the independent "oscillatory motion" calibration.

PSF modeling

The point spread function (PSF) as reconstructed from $\mathcal{M}$ [7] is shown in Fig. S7. The imaging imperfections are taken into account by convolving the 2D profile of the density predicted by the theory with the PSF. We estimate the systematic error in the determination of the EoS by varying the HWHM of the reconstructed PSF. Testing the sensitivity of the fit parameter results, we find that, in the deep Mott insulating regime, where the effects of the PSF are most relevant, a variation of 50 % in the size of the HWHM causes only a change of 4 % in the entropy [for $U/t = 33(2)$ and $N = 6$].

F. Fit method and parameters for the EoS

We fit a 2D model of the density with fixed κ_x, κ_y and cross section determined with a separate fit as described in Sec. S.I D 1 and S.I E. Due to small position fluctuations during imaging, we perform an initial fit of each image to determine the center of the trap. We use this

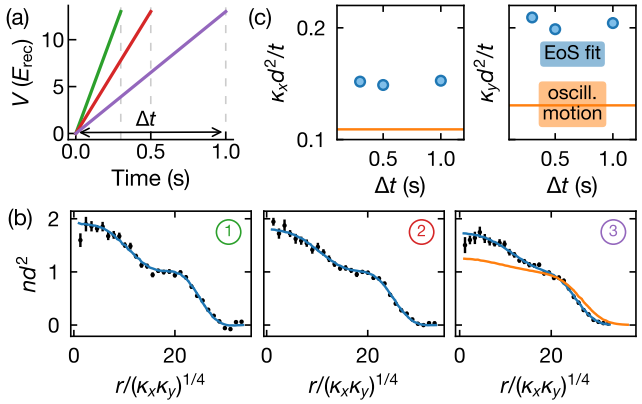

FIG. S6. Robustness of the EoS fit as a function of the ramp duration. (a) We tune a SU(6) sample to $U/t \approx 44$ with a linear ramp of duration $\Delta t = 0.3\,\mathrm{s}$ (green), $0.5\,\mathrm{s}$ (red), $1\,\mathrm{s}$ (purple). (b) For each ramp duration Δt, we fit the density profile assuming an harmonic potential with coefficients determined by the "oscillatory-motion" calibration (orange) and by leaving the coefficients free in the EoS fit (blue). Here, we plot the results of the fit with respect to the spacial radial profile. For the first two frames, the "oscillatory-motion" fit fails. (c) Comparison of the harmonic potential coefficients.

to align the centers of the distributions and perform a fit of the average of several realizations with similar atom number (15 realizations for the dataset of Fig. 2).

In Tab. S2 we report the values returned by the EoS fit shown in Fig. 2 and a comparison between different numerical methods.

The fit results do not take into account the uncertainties on U/t. By fitting different values of U/t to the same data, we estimate the systematic error on the entropy per particle and the temperature to be about 1% and $0.015\,U$ respectively.

G. Equation of state for higher temperatures

In Fig. S8 we probe the equation of state as a function of the initial entropy for $N = 6$. We increase the entropy by holding the atoms in the 2D bulk before the lattice ramps. In this way, we can vary the entropy per particle s between approximately $1\,k_\mathrm{B}$ and $2\,k_\mathrm{B}$ (grey squares). After loading into the lattices, we fit the density and compare different numerical methods, including DQMC, NLCE and HTSE. For high initial entropy and large interactions, the methods agree very well with each other. For lower initial entropy, first HTSE and then NLCE begin to deviate. We also perform a round-trip experiment as described in the main text (grey crosses). For large initial entropies, we observe a good agreement between the entropies in the lattice and after the round trip experiment, indicating that the increase is mainly occurring during the ramp up.

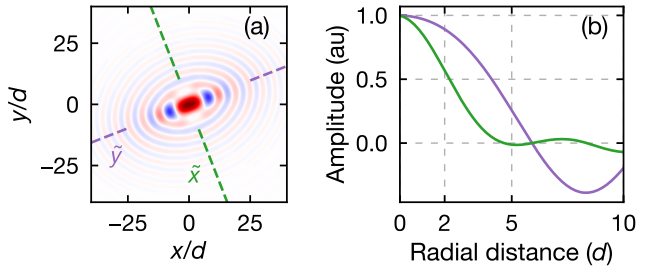

FIG. S7. (a) Reconstructed point spread function (PSF). x and y have been labeled according to the convention defined in Fig. 1. The color scale is in arbitrary units and varies between -1 (blue) and 1 (red). (b) Cuts along the main axes of the PSF [dashed lines in (a)].

H. Equation of state in the bulk

The entropy per particle in 2D prior to turning on the in-plane lattices is calculated from a fit of the equation of state for a weakly-interacting Fermi gas. In particular, we obtain the temperature from the fit of the in situ density according to:

$$n(\mu, T) = -\frac{\partial \Omega}{\partial \mu} = -N\frac{m}{2\pi\hbar^2\beta}\mathrm{Li}_1(-e^{\beta\mu}), \qquad \text{(S.5)}$$

where Ω is the grand potential, Li_1 is the polylogarithm of order 1, $\beta = 1/(k_\mathrm{B}T)$, and m is the mass of one ^{173}Yb atom. The harmonic potential is taken into account in local density approximation. The effect of interactions is taken into account by introducing a correction to the chemical potential [10]:

$$\mu_\mathrm{int}(\beta) \approx \frac{1}{\beta}\left[1 + 2g(N-1) + 4g^2(N-1)(1-\log 2)\right]\log\left(e^{\beta E_\mathrm{F}} - 1\right), \qquad \text{(S.6)}$$

where E_F is the Fermi energy and g is the interaction parameter:

$$g(n, N) = \frac{1}{\log 2 - 2\log\left(k_\mathrm{F} a_\mathrm{2D}\right)}. \qquad \text{(S.7)}$$

Here, $k_\mathrm{F} = \sqrt{4\pi n/N}$ is the local Fermi vector and $a_\mathrm{2D} \simeq 2.5 \times 10^{-3}\,\mathrm{a_0}$ is the 2D scattering length. The density-dependency of the interaction parameter is evaluated self-consistently in the fit routine similarly to what has been done in 3D in Ref. [11]. We convolve the predicted density profile with the PSF to take into account imaging imperfections. The entropy is calculated from the temperature returned by the fit and the spectrum of the 3D non-isotropic harmonic oscillator [12]. We determine a correction to the entropy due to the interactions between 5 % and 20 % compared to the one returned by the fit of a non-interacting Fermi profile.

N	U/t	N_p ($\times 10^3$)	Method	T/t	T/U	s/k_B
3	2.3(1)	1.98(2)	DQMC	0.40(4)	0.17(2)	
	7.5(4)	1.96(2)	NLCE-6	1.24(3)	0.167(4)	1.50(6)
			NLCE-7	1.24(3)	0.167(4)	1.50(6)
	10.4(6)	1.94(3)	NLCE-6	1.69(4)	0.163(4)	1.55(6)
			NLCE-7	1.69(4)	0.163(4)	1.55(6)
			HTSE-2	1.69(4)	0.163(4)	1.56(6)
	33(2)	1.99(2)	NLCE-6	5.0(1)	0.149(3)	1.51(4)
			NLCE-7	5.0(1)	0.149(3)	1.51(4)
			HTSE-2	5.0(1)	0.149(3)	1.51(4)
4	2.3(1)	1.99(1)	DQMC	0.32(3)	0.13(1)	
	7.5(4)	1.99(1)	DQMC	0.97(3)	0.130(4)	1.61(7)
			NLCE-4	0.98(3)	0.131(3)	1.59(6)
			NLCE-5	0.94(3)	0.126(4)	1.57(7)
	10.4(6)	1.99(1)	DQMC	1.36(4)	0.131(4)	1.73(6)
			NLCE-4	1.42(4)	0.137(4)	1.73(6)
			NLCE-5	1.41(4)	0.136(4)	1.72(6)
			HTSE-2	1.43(4)	0.138(3)	1.76(7)
	33(2)	1.99(1)	NLCE-4	4.62(9)	0.139(3)	1.78(5)
			NLCE-5	4.62(9)	0.139(3)	1.78(5)
			HTSE-2	4.63(9)	0.139(3)	1.78(5)
6	2.3(1)	1.99(1)	DQMC	0.30(1)	0.127(1)	
	7.5(4)	1.99(1)	DQMC	0.91(3)	0.122(4)	1.95(9)
			NLCE-3	0.94(3)	0.126(4)	1.97(8)
			NLCE-4	0.91(2)	0.122(3)	1.90(7)
	10.4(6)	2.05(1)	DQMC	1.35(4)	0.131(4)	2.11(8)
			NLCE-3	1.40(4)	0.135(3)	2.10(8)
			NLCE-4	1.38(4)	0.133(4)	2.08(8)
			HTSE-2	1.48(3)	0.142(3)	2.15(9)
	33(2)	2.00(1)	NLCE-3	3.99(8)	0.120(2)	2.12(6)
			NLCE-4	3.99(8)	0.120(2)	2.12(6)
			HTSE-2	4.06(8)	0.122(2)	2.13(6)

TABLE S2. Fit parameters for the EoS shown in Fig. 2 and comparison between different methods. For each sample, we consider 15 shots postselected according to the total atom number. For HTSE and NLCE methods, the number indicates the order. The agreement between two consecutive orders indicates that NLCE has converged. In Fig. 2 we plot the highest NLCE order if available, DQMC otherwise. The uncertainties correspond to the values returned by the fit and do not take into account additional systematic errors.

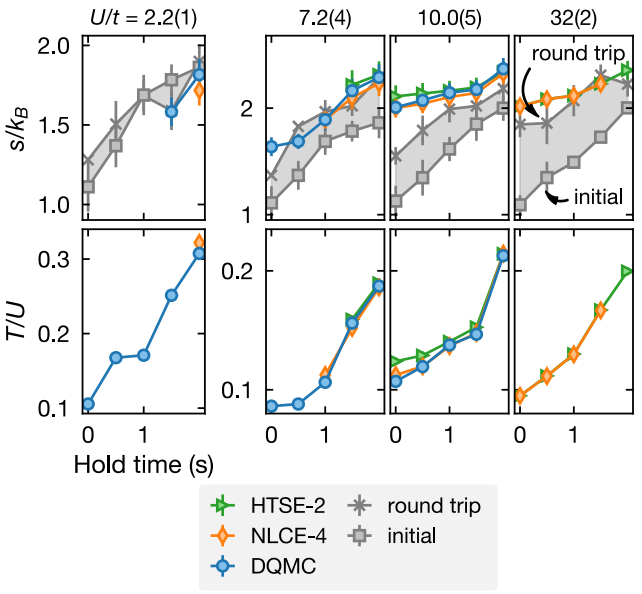

FIG. S8. Equation of state for high temperature for $N = 6$. By varying the hold time in the 2D bulk before ramping up the lattices, we increase the initial entropy per particle (grey squares). After loading into the lattice, we perform a fit of the density obtained by the average of 15 frames with $N_p \approx 2.2 \times 10^3$ and a s.e.m. of 15 to 35 for each combination of U/t and hold time, after atom number postselection and COM alignment. We fit the same datapoint with different methods and compare the results. We fit DQMC (blue circles), NLCE of order 4 (orange diamonds) and HTSE of order 2 (green triangles). After loading into the lattice we perform a round-trip experiment by symmetrically ramping down the lattices and measuring the entropy in the bulk (grey crosses). For this measurement, the vertical bandgap was $h \times 3.63(1)\,\mathrm{kHz}$ and the confinement's parameters κ_x and κ_y have been calibrated according to the same method presented in the main text (for $N = 6$ only).

I. Fluctuations

1. *Binning, PSF and shot noise*

We spatially bin each frame in square "superpixels" and compute the chemical potential μ and the local density variance in each of them.

We take into account the PSF originating from the binning by measuring the density fluctuations for a SU(6) thermal cloud ($T \gg T_F$) in the bulk with the same binning. For a non-interacting cloud with point-like PSF and $T/T_F \gg 1$, $\mathrm{var}(\hat{n})/\langle\hat{n}\rangle \simeq 1$. The binning lowers this ratio, which can be used as a calibration scaling factor for the fluctuations in the lattice. However, we also take into account additional corrections due to the temperature and the interactions in the bulk. We do so by fitting the cloud with a weakly-interacting model (see Sec. S.I H) and determine $T/T_F = 1.02(1)$. For this temperature and interaction strength, we expect $\mathrm{var}(\hat{n})/\langle\hat{n}\rangle \equiv \xi_\infty = 0.69(1)$ for small densities (see Fig. S9). The binning to finite-size superpixels introduces an additional correction $\xi_\infty \to \xi_i$, where i is the linear size of the superpixel. For $4\,\mathrm{px} \times 4\,\mathrm{px}$ superpixels, the size that we use in Fig. 3, we measure the correction $\xi_4 = 0.39(1)$.

In the lattice, we first do the binning, then subtract the photon shot noise as the average density at the edge of the region of interest and finally rescale the variance by the factor $\left(\xi_4\,\sigma^{\mathrm{bulk}}/\sigma^{\mathrm{lat}}\right)^{-1}$, which also takes into account the correction to the cross section described in Sec. S.I E.

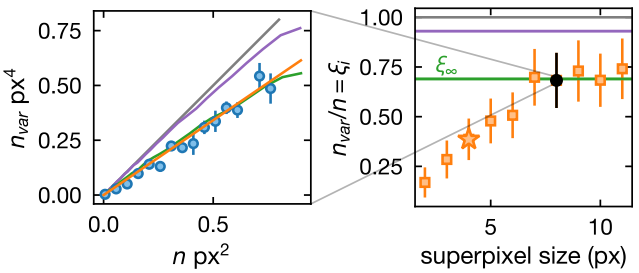

FIG. S9. Fluctuations in the bulk for $N = 6$. Left: density variance calculated with superpixels of size 8 px × 8 px. Blue points: measured density variance. Grey line: for a thermal, non-interacting cloud $\mathrm{var}(n)/n = 1$. Purple line: theoretical prediction estimated from the temperature returned by a non-interacting Fermi fit [$T/T_F = 1.37(1)$]. Green line: theoretical prediction according to a weakly-interacting Fermi fit [$T/T_F = 1.02(1)$]. Orange line: linear fit of the measured density fluctuations. Right: slope $n_{\mathrm{var}}/n = \xi_i$ returned by the linear fit as a function of the superpixel size i [$(i \times i)$ px^2 is the superpixel area]. Star ($i = 4$): superpixel size used in the lattice.

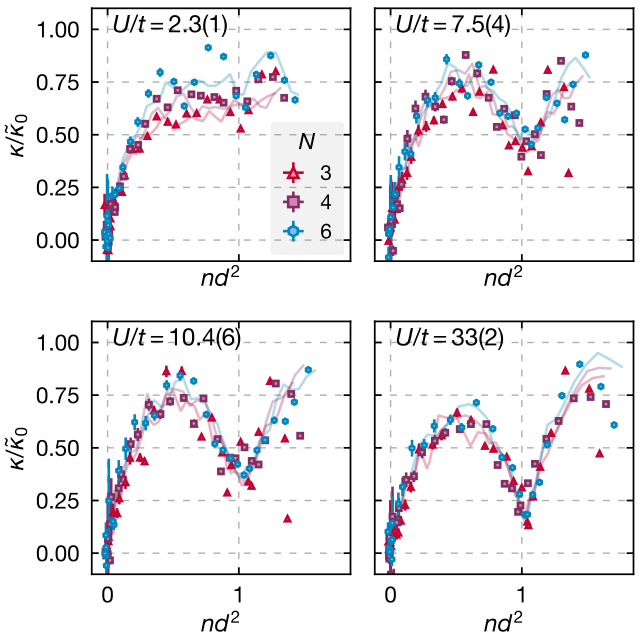

FIG. S10. Isothermal compressibility $\kappa = \partial n/\partial\mu|_T$ for $N = 3$ (red), $N = 4$ (purple), and $N = 6$ (blue). $\tilde{\kappa}_0$ is the compressibility of a SU(6) non-interacting gas at zero temperature. For each combination of N and U/t, we numerically differentiate the density with respect to the chemical potential. The dataset is the same as Figs. 2 and 3. Points correspond to the differentiation of the experimental data and lines correspond to the differentiation of the theoretical curves.

2. *Compressibility*

To calculate the isothermal compressibility $\kappa = \partial n/\partial\mu|_T$, we first bin the experimental data in 1D as $n(\mu)$ and then numerically perform a 3-point differentiation. Fig. S10 shows the compressibility for the $N = 6$ dataset of Fig. 3 and a comparison with the datasets for $N = 3$ and 4 shown in Fig. 2.

3. *FDT Thermometry*

In order to extract the temperature from the FDT, we linearly interpolate the compressibility (Sec. S.II 2) to match the binning grid of the density fluctuations (Sec. S.II 1) and calculate the local temperature as the ratio between the local variance and compressibility. The global temperature T_{FDT} is calculated as weighted average of the local temperature as a function of the chemical potential for $nd^2 > 0.05$. In Fig. S11, we show the local temperature and compare it to T_{FDT} and T_{EoS} for $N = 6$.

4. *Fluctuations for $N = 3$ and 4*

In Fig. S12 and S13 we show the density fluctuations and the comparison between T_{EoS} and T_{FDT} for $N = 4$ and 3 respectively. In the case of $N = 4$, we show a dataset with a larger number of frames compared to what has been used in Fig. 3 (35 frames instead of 15) with similar s.e.m. in the total atom number to narrow down the error bar on T_{FDT} and allow for a more precise comparison.

S.II. NUMERICAL METHODS

In this section we present details of the DQMC and NLCE calculations used for results in the main text, including estimates of systematic errors, and a derivation of the HTSE.

A. Determinantal Quantum Monte Carlo

Averages of the thermal equilibrium observables are evaluated with Determinantal Quantum Monte Carlo (DQMC) [13, 14] on 6×6 lattices by introducing $N(N-1)/2$ auxiliary Hubbard-Stratonovich fields, one for each interaction term [15, 16] [1]. In this method, the inverse temperature β is discretized in steps of $\Delta\tau$ (Trotter steps). Results in the main text use $\Delta\tau = 0.05/t$. We obtain DQMC data for 5 different random initial seeds

[1] Previous work applied DQMC for the SU($2N$) Fermi-Hubbard model at half-filling, i.e. $\langle n \rangle = N/2$, using an alternative Hubbard-Stratonovitch decomposition. This alternative decomposition is free of the sign problem at half-filling for SU($2N$) [17–20].

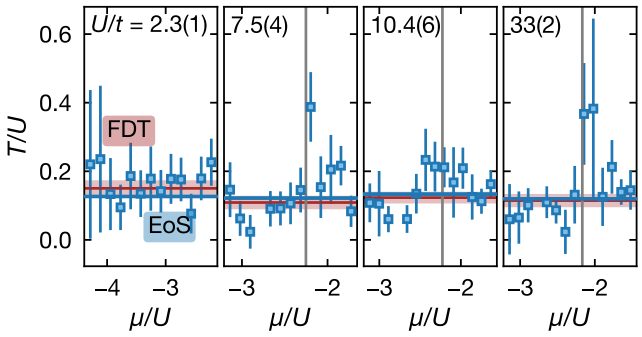

FIG. S11. Local temperature for the $N = 6$ dataset shown in Fig. 3. Blue line: temperature according to the fit of the EoS. Red line: temperature according to the fit of the FDT. Vertical line: $\mu(nd^2 = 1)$. The local temperature for small and large densities is in general comparable, hinting at global thermal equilibrium.

for $U/t = 7.43, 10.38$ and for 20 different random seeds for $U/t = 2.34$. For each Monte Carlo trajectory we perform 2000 warm up sweeps through the whole space-time lattice and 8000 sweeps for measurements. Furthermore, we use 4 global moves per sweep to ensure ergodicity [21].

In addition to statistical errors, (controllable) systematic errors can arise from the finite Trotter step, finite-size effects, and imperfect equilibration of the Monte Carlo algorithm before measurement. The Trotter error obtained by comparing $\Delta\tau = 0.04/t$ and $\Delta\tau = 0.05/t$ results is $\lesssim 0.03\,t$ for the temperature and $\lesssim 0.06\,k_B$ for the entropy across all N and U/t considered. These correspond to relative errors that are $\lesssim 8\%$, and in all cases are smaller than the statistical error bars [2]. The finite-size error assessed by taking the difference of temperature and entropy obtained from fits using results from 4×4 and 6×6 lattices is $\lesssim 0.04\,t$ for the temperature and $\lesssim 0.03\,k_B$ for the entropy for all N and U/t considered, except for $N = 6$ at $U/t = 2.34$ where the errors are $0.07\,t$ and $0.13\,k_B$. The equilibration error is negligible in the homogeneous case and was estimated by comparing results using 2000 and 8000 warm up sweeps. This error is $\lesssim 0.002$ for the density and $\lesssim 0.04\,t$ for the energy across all chemical potentials considered in the homogeneous case.

DQMC results are calculated on a grid of μ and T, which can also introduce systematic errors into the fits of the experimental equation of state measurements to theory. We use a grid with $\mathrm{d}\mu = 0.25\,t$ and $\mathrm{d}T/t \sim 0.05$ for $T/t \leq 0.6$, and $\mathrm{d}T/t \sim 0.1$ for $0.6 \leq T/t \leq 1.5$. Effects due to the coarseness of the μ grid were estimated by considering differences of temperature and entropy fits using $\mathrm{d}\mu = 0.25\,t$ and $\mathrm{d}\mu = 0.5\,t$ and are $\lesssim 0.007\,t$ and $\lesssim 0.05\,k_B$.

[2] For results at $U/t = 7.43$ and 10.38, relative errors are $\sim 1\%$.

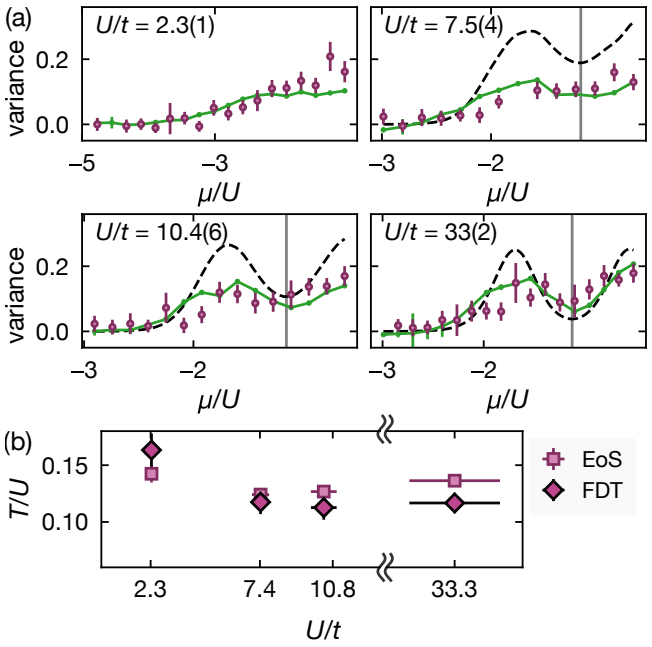

FIG. S12. (a) Measured density fluctuations (purple) for $N = 4$ as a function of the chemical potential for different interaction strengths. The data points have been obtained from the variance of 35 frames according to the same binning and evaluation method of Fig. 3. The green line corresponds to the numerically-differentiated compressibility κ times the temperature T_{EoS} obtained from the EoS-fit of the averaged data. The vertical line indicates $\mu(nd^2 = 1)$. The dashed line corresponds to the on-site density fluctuations $\delta n_0^2 = \langle \hat{n}^2 \rangle - \langle \hat{n} \rangle^2$ calculated with NLCE for T_{EoS}. (b) Comparison of the temperatures T_{FDT} (dark purple diamonds) and T_{EoS} (light purple squares). Error bars are the s.e.m.

Convergence criteria correspond to the lowest T/t for which fluctuations in entropy for two consecutive μ data points still fall within statistical error bars.

B. Numerical Linked Cluster Expansion

Thermodynamic observables are computed using site expansion Numerical Linked Cluster Expansion (NLCE) up to seventh order (seven sites) for SU(3), fifth order for SU(4) and fourth order for SU(6) Fermi-Hubbard models. A brief discussion of the algorithm is presented below. Extensive properties of a lattice $\mathcal{L}$ are computed by performing a weighted sum of the property values over all embeddable clusters c [22, 23]. Formally,

$$P(\mathcal{L})/N_s = \sum_{c \subset \mathcal{L}} L(c) W_P(c) \tag{S.8}$$

where $P(\mathcal{L})$ is the lattice property, N_s is the number of lattice sites, $L(c)$ is the number of ways per site the clus-

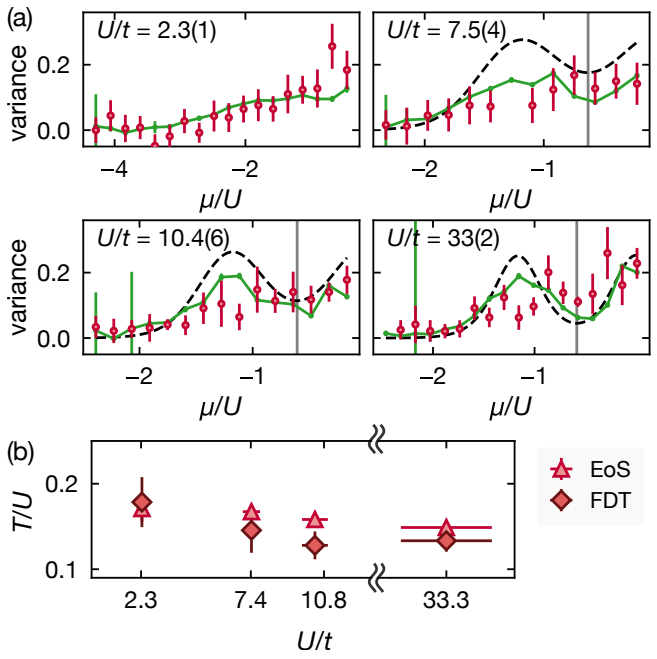

FIG. S13. (a) Measured density fluctuations (red) for $N = 3$ as a function of the chemical potential for different interaction strengths. The data points have been obtained from the variance of 15 frames according to the same binning and evaluation method of Fig. 3. The green line corresponds to the numerically-differentiated compressibility κ times the temperature $T_{\rm EoS}$ obtained from the EoS-fit of the averaged data. The vertical line indicates $\mu(nd^2 = 1)$. The dashed line corresponds to the on-site density fluctuations $\delta n_0^2 = \langle \hat{n}^2 \rangle - \langle \hat{n} \rangle^2$ calculated with NLCE for $T_{\rm EoS}$. (b) Comparison of the temperatures $T_{\rm FDT}$ (dark red diamonds) and $T_{\rm EoS}$ (light red triangles). Error bars are the s.e.m.

ter c can be embedded in the lattice $\mathcal{L}$, and the weights $W_P(c)$ are defined as

$$W_P(c) = P(c) - \sum_{s \subset c} W_P(s) \tag{S.9}$$

where $P(c)$ is computed by performing exact diagonalization of the Hamiltonian in Eq. 1 defined over the cluster c. The Hilbert space dimension grows exponentially with both system size N_s and number of spin flavors N. We use spin flavor conservation symmetry to reduce the Hilbert space dimension as mentioned in Ref. [15].

Note that Eq. S.8 follows from Eq. S.9 applied to $c = \mathcal{L}$. The NLCE works by truncating Eq. S.8 to a finite order (finite number of sites in the clusters included), which yields accurate results when correlation lengths are sufficiently short, as happens when temperature is not too low. The NLCE is typically much more accurate than exact diagonalization employing the same number of sites. See the Appendix of Ref. [15] for a comparison of bare ED and NLCE for the SU(N) Hubbard model. The NLCE converges to lower temperatures when the density is an integer, and when U/t is larger. For both cases, the system has shorter-ranged correlations at a fixed temperature and thus the system properties are captured by small clusters.

The only error in the NLCE arises from truncating Eq. S.8 to finite cluster size. We evaluate this by comparing properties calculated with successive orders of the NLCE approximation. When two orders of NLCE consistently agree, generally the result is converged and the value equals that in the thermodynamic limit [23].

The NLCE was computed over T/t grid of 500 points linearly spaced in the range $[0.5, 10]$, i.e. $\mathrm{d}T/t \sim 0.02$. The μ/t grid was varied for different U/t and N such that the density, $\langle n \rangle \in [0, N/2]$. For each U/t and N, there are 500 μ/t-points. In the main text (Fig. 2), the chemical potential is re-scaled with U, thus the μ-spacing $\mathrm{d}\mu/U$ varies between 0.01 and 0.02. The choice of the temperature and chemical potential grids was made to get a dense enough grid to get small fit errors to the experimental data (Fig. 2).

C. High Temperature Series Expansion

We also present results from a second-order high temperature series expansion (HTSE) in t/T which is accurate for $T \gtrsim t$. In the following, subscripts are used to indicate the expansion's order in t/T for the different physical quantities $\langle O \rangle_\ell$.

1. *Zeroth-order HTSE ($t = 0$)*

The energy as a function of the occupation of a single site in the grand canonical ensemble is given by,

$$\epsilon_0(n) = \frac{U}{2} n(n-1) - \mu n + g\delta_{n,\alpha}, \tag{S.10}$$

where we introduced the last term to allow extraction of the p_α by differentiating the partition function with respect to g. The partition function for the single site is given by $z_0 = \sum_{n=0}^{N} \binom{N}{n} e^{-\beta\epsilon_0(n)}$, and the grand canonical free energy per site is $\Omega_0 = -T \ln z_0$. For compactness, we define $y = e^{-\beta U}$, $x = e^{\beta\mu}$, and $w = e^{-\beta g}$.

In the zeroth-order HTSE $\langle p_\alpha \rangle_0 = \lim_{g\to 0} \frac{\partial \Omega_0}{\partial g}$, which gives

$$\langle p_\alpha \rangle_0 = \frac{\binom{N}{\alpha} y^{\frac{1}{2}\alpha(\alpha-1)} x^\alpha}{\sum_{n=0}^{N} \binom{N}{n} y^{\frac{1}{2}n(n-1)} x^n}. \tag{S.11}$$

The density $\langle n \rangle_0$ and number of on-site pairs $\langle \mathcal{D} \rangle_0 = \langle n(n-1)/2 \rangle_0$ are related to $\langle p_\alpha \rangle_0$ via $\langle n \rangle_0 = \sum_{\alpha=1}^{N} \alpha \langle p_\alpha \rangle_0$, and $\langle \mathcal{D} \rangle_0 = \sum_{\alpha=2}^{N} \binom{\alpha}{2} \langle p_\alpha \rangle_0$.

2. Second-order HTSE

The first correction to the free energy is second-order in t/T, i.e. $\Omega_2 = \Omega_0 + \Delta\Omega$ [24], where $\Delta\Omega$ is presented in Refs. [5, 25, 26] for $g = 0$. For general g we find

$$-\beta\Delta\Omega = qN\left(\frac{\beta t}{z_0}\right)^2\left[\frac{1}{2}\sum_{n=1}^{N}\binom{N-1}{n-1}^2 x^{2n-1}y^{(n-1)^2}w^{\delta_{\alpha,n}+\delta_{\alpha,n-1}} - \frac{1}{\beta U}\sum_{n\neq m}\binom{N-1}{n-1}\binom{N-1}{m-1}\frac{x^{n+m-1}y^{\frac{1}{2}[n(n-1)+(m-1)(m-2)]}w^{\delta_{\alpha,n}+\delta_{\alpha,m-1}}}{n-m}\right], \tag{S.12}$$

where q is the coordination number. Following the same procedure as before, $\langle p_\alpha\rangle_2 = \langle p_\alpha\rangle_0 + \langle\Delta p_\alpha\rangle$, where $\langle\Delta p_\alpha\rangle$ is given by $\langle\Delta p_\alpha\rangle = \lim_{g\to 0}\frac{\partial\Delta\Omega}{\partial g}$, yielding

$$\langle\Delta p_\alpha\rangle = qN\left(\frac{\beta t}{z_0}\right)^2\left[\frac{1}{2}\sum_{n=1}^{N}\binom{N-1}{n-1}^2 x^{2n-1}y^{(n-1)^2}\big(-2\langle p_\alpha\rangle_0+\delta_{\alpha,n}+\delta_{\alpha,n-1}\big) - \frac{1}{\beta U}\sum_{n\neq m}\binom{N-1}{n-1}\binom{N-1}{m-1}\frac{x^{n+m-1}y^{\frac{1}{2}[n(n-1)+(m-1)(m-2)]}}{n-m}\big(-2\langle p_\alpha\rangle_0+\delta_{\alpha,n}+\delta_{\alpha,m-1}\big)\right]. \tag{S.13}$$

The second order expectations $\langle n\rangle_2$ and $\langle\mathcal{D}\rangle_2$ are related to $\langle p_\alpha\rangle_2$ via $\langle n\rangle_2 = \sum_{\alpha=1}^{N}\alpha\langle p_\alpha\rangle_2$, and $\langle\mathcal{D}\rangle_2 = \sum_{\alpha=2}^{N}\binom{\alpha}{2}\langle p_\alpha\rangle_2$, respectively.

* giulio.pasqualetti@lmu.de

[1] A. Impertro, *Preparation and study of 1D and 2D Many-Body Systems with Fermionic Ytterbium*, Master's thesis, Ludwig-Maximilians-Universtät München (2020).

[2] K. Hueck, N. Luick, L. Sobirey, J. Siegl, T. Lompe, and H. Moritz, Two-dimensional homogeneous fermi gases, Physical Review Letters **120**, 060402 (2018).

[3] S. Stellmer, R. Grimm, and F. Schreck, Detection and manipulation of nuclear spin states in fermionic strontium, Physical Review A **84**, 043611 (2011).

[4] D. Jaksch, C. Bruder, J. I. Cirac, C. W. Gardiner, and P. Zoller, Cold bosonic atoms in optical lattices, Physical Review Letters **81**, 3108 (1998).

[5] C. Hofrichter, L. Riegger, F. Scazza, M. Höfer, D. R. Fernandes, I. Bloch, and S. Fölling, Direct probing of the Mott crossover in the SU(N) Fermi-Hubbard model, Physical Review X **6**, 021030 (2016).

[6] G. Reinaudi, T. Lahaye, Z. Wang, and D. Guéry-Odelin, Strong saturation absorption imaging of dense clouds of ultracold atoms, Optics Letters **32**, 3143 (2007).

[7] C.-L. Hung and C. Chin, In situ imaging of atomic quantum gases, in *Quantum Gas Experiments: Exploring Many-Body States*, Vol. 3 (Imperial College Press, London, 2014) Chap. 6, p. 101.

[8] L. Chomaz, L. Corman, T. Yefsah, R. Desbuquois, and J. Dalibard, Absorption imaging of a quasi-two-dimensional gas: A multiple scattering analysis, New Journal of Physics **14**, 055001 (2012).

[9] J. Rui, D. Wei, A. Rubio-Abadal, S. Hollerith, J. Zeiher, D. M. Stamper-Kurn, C. Gross, and I. Bloch, A subradiant optical mirror formed by a single structured atomic layer, Nature **583**, 369 (2020).

[10] J. R. Engelbrecht, M. Randeria, and L. Zhang, Landau f function for the dilute Fermi gas in two dimensions, Physical Review B **45**, 10135 (1992).

[11] L. Sonderhouse, C. Sanner, R. B. Hutson, A. Goban, T. Bilitewski, L. Yan, W. R. Milner, A. M. Rey, and J. Ye, Thermodynamics of a deeply degenerate SU(N)-symmetric Fermi gas, Nature Physics **16**, 1216 (2020).

[12] M. Köhl, Thermometry of fermionic atoms in an optical lattice, Physical Review A **73**, 031601(R) (2006).

[13] R. Blankenbecler, D. J. Scalapino, and R. L. Sugar, Monte Carlo calculations of coupled boson-fermion systems. I, Physical Review D **24**, 2278 (1981).

[14] S. Sorella, S. Baroni, R. Car, and M. Parrinello, A novel technique for the simulation of interacting fermion systems, Europhysics Letters (EPL) **8**, 663 (1989).

[15] E. Ibarra-García-Padilla, S. Dasgupta, H.-T. Wei,

S. Taie, Y. Takahashi, R. T. Scalettar, and K. R. A. Hazzard, Universal thermodynamics of an SU(N) Fermi-Hubbard model, Physical Review A **104**, 043316 (2021).
[16] S. Taie, E. Ibarra-García-Padilla, N. Nishizawa, Y. Takasu, Y. Kuno, H.-T. Wei, R. T. Scalettar, K. R. A. Hazzard, and Y. Takahashi, Observation of antiferromagnetic correlations in an ultracold SU(N) Hubbard model, Nature Physics **18**, 1356 (2022).
[17] F. F. Assaad, SU(2)-spin invariant auxiliary field quantum Monte Carlo algorithm for Hubbard models, cond-mat/9806307 (1998), arXiv:cond-mat/9806307.
[18] D. Wang, Y. Li, Z. Cai, Z. Zhou, Y. Wang, and C. Wu, Competing orders in the 2D half-filled SU(2N) Hubbard model through the pinning-field quantum Monte Carlo simulations, Physical Review Letters **112**, 156403 (2014).
[19] Z. Zhou, Z. Cai, C. Wu, and Y. Wang, Quantum Monte Carlo simulations of thermodynamic properties of SU(2N) ultracold fermions in optical lattices, Physical Review B **90**, 235139 (2014).
[20] F. F. Assaad, Phase diagram of the half-filled two-dimensional SU(N) Hubbard-Heisenberg model: A quantum Monte Carlo study, Physical Review B **71**, 075103 (2005).
[21] R. T. Scalettar, R. M. Noack, and R. R. P. Singh, Ergodicity at large couplings with the determinant Monte Carlo algorithm, Physical Review B **44**, 10502 (1991).
[22] M. Rigol, T. Bryant, and R. R. P. Singh, Numerical linked-cluster approach to quantum lattice models, Physical Review Letters **97**, 187202 (2006).
[23] B. Tang, E. Khatami, and M. Rigol, A short introduction to numerical linked-cluster expansions, Computer Physics Communications **184**, 557 (2013).
[24] J. Oitmaa, C. Hamer, and W. Zheng, *Series Expansion Methods for Strongly Interacting Lattice Models* (Cambridge University Press, Cambridge, 2006).
[25] K. R. A. Hazzard, V. Gurarie, M. Hermele, and A. M. Rey, High-temperature properties of fermionic alkaline-earth-metal atoms in optical lattices, Physical Review A **85**, 041604(R) (2012).
[26] S. Taie, R. Yamazaki, S. Sugawa, and Y. Takahashi, An SU(6) Mott insulator of an atomic Fermi gas realized by large-spin Pomeranchuk cooling, Nature Physics **8**, 825 (2012).